Modeling of the groundwater flow system in excavated areas of an abandoned mine

Shingo Tomiyama[a,b,*], Toshifumi Igarashi[a], Carlito Baltazar Tabelin[c], Pawit Tangviroon[a], Hiroyuki Ii[d]

a Division of Sustainable Resources Engineering, Faculty of Engineering, Hokkaido University, Kita 13 Nishi 8, Sapporo, Japan 060-8628

b Mitsubishi Materials Corporation, 3-2-3, Marunouchi, Chiyoda-ku, Tokyo, Japan 100-8117

c School of Minerals and Energy Resources Engineering, Faculty of Engineering, the University of New South Wales, Sydney, NSW 2052, Australia

d Graduate School of Systems Engineering, Wakayama University, 930 Sakaedani, Wakayama, Japan 640-8510

*Corresponding author

e-mail: tomiyama@mmc.co.jp

phone: +81-11-706-8191

1. Introduction

Acid mine drainage (AMD) or acid rock drainage (ARD) fluids are generally characterized by low pH and very high concentrations of sulfate, heavy metals (e.g., copper (Cu), lead (Pb), zinc (Zn), and cadmium (Cd)), and toxic metalloids (e.g., arsenic (As) and selenium (Se)), which pose serious threats when released without appropriate

25 treatment, not only to the environment, but also to residents living around the affected
26 areas (Tabelin et al., 2018). AMD is typically associated with many active, closed, and
27 abandoned mines (Younger, 2001; Gault et al., 2005; Molson et al., 2005; Boulabah et
28 al., 2006; Kimball et al., 2007; Lim et al., 2008; Hien et al., 2012; Hierro et al., 2014;
29 Skierszkan et al., 2016; Zhao et al., 2017). ARD is also a major problem in many
30 underground and tunnel construction projects when the excavated debris and/or waste
31 rocks contain pyrite, which is the most abundant sulfide mineral in nature and the
32 primary cause of acidic leachate formation (Tabelin and Igarashi, 2009; Tabelin et al.,
33 2012a,b, 2013, 2017a,b; Tatsuhara et al., 2012; Andrea, 2014; Anawar, 2015).
34 The most common mitigation strategy for AMD–ARD is chemical neutralization,
35 which is a method whereby the acidic effluents are mixed with alkaline materials like
36 limestone, lime, or caustic soda to raise the pH and precipitate most of the heavy metals
37 and metalloids (Iakovleva et al., 2015). Although effective, the long-term suitability of
38 this approach depends on the volume and geochemical properties of the AMD–ARD
39 being treated, as well as the total duration of treatment required at a specific site. As
40 such, the treatment becomes costly and unsustainable because AMD–ARD contain high
41 concentrations of heavy metals and are generated over a long period (>100 yr). The
42 generation of large amounts of sludge that must be properly managed is also an
43 important issue. Several advanced pyrite passivation techniques have been recently
44 proposed for more sustainable management of AMD–ARD, such as carrier
45 microencapsulation (Satur et al., 2007; Park et al., 2018a,b; Li et al., 2019) and galvanic
46 microencapsulation (Tabelin et al., 2017c), which show selectivity for pyrite and
47 arsenopyrite, even in the presence of silicates. However, these techniques are still in the
48 experimental stages and remain untested under *in situ* conditions. Given this, the

sustainability of existing AMD–ARD management strategies should be improved until more effective and sustainable methods are developed.

One potential way to improve the sustainability of current AMD–ARD treatment strategies is to limit the formation of acidic leachates at source by the application of hydrogeological methods (e.g., ground-sealing with low permeability materials) that reduce the amount of water in contact with pyrite-rich waste or wall rocks. In addition, covers with oxygen-barrier effects have been proposed as a viable option to minimize AMD, whilst also controlling gas flow and oxygen supply (Bussière et al., 2003; Lahmira et al., 2016). Some of these approaches could reduce the capacity of current water treatment plants or wetland-based treatment methods, by not only reducing the volume, but also improving the quality of AMD for treatment. However, for this approach to work, it is crucial to first understand both the sources and flow patterns of AMD–ARD within the mining area. The sources of AMD–ARD are typically identified by detailed geochemical and isotopic surveys of the target mine, which have been conducted in Japan (Iwatsuki and Yoshida, 1999; Okumura, 2003; Mahara et al., 2006) and in other countries (Razowska, 2001; Hazen et al., 2002; Sracek et al., 2004; Lee and Chon, 2006; Leybourne et al., 2006; Hubbard et al., 2009; Gammons et al., 2010; Galván et al., 2016; Cánovas et al., 2017; Migaszewski et al., 2018). In addition, AMD–ARD flow patterns can be predicted by combining numerical models with on-site hydrological surveys.

Once the sources of AMD are known and its flow patterns established, various countermeasures to limit the flow of AMD or retard the movement of contaminants could be evaluated using numerical models calibrated to on-site data. When properly calibrated, numerical models are capable of reproducing the groundwater flow in and

around the mine site and changes in these flow patterns in response to various environmental parameters (e.g., changes in rainfall intensity). For example, several studies have successfully predicted both the geochemical evolution of groundwater (Bain et al., 2000; Molson et al., 2005; Castendyk and Webster-Brown, 2007; Yamaguchi et al., 2015; Pabst et al., 2018) and its movement through natural geological media using numerical modeling techniques (Wunsch et al., 1999; Sracek et al., 2004; Tomiyama et al., 2010a, 2010b, 2016; Bahrami et al., 2016; Ethier et al., 2018; Ramasamy et al., 2018).

One of the biggest challenges in the simulation of groundwater flow in closed and/or abandoned underground mines is how to consider a number of large excavated spaces and tunnels in the numerical model. For example, in a study of the Kamaishi mine (a skarn-type deposit), the modeling approach assumed that the excavated areas were hollow spaces with groundwater discharge by setting the walls as a fixed total head boundary (Japan Nuclear Cycle Development Institute, 1999). Modeling of underground oil storage in Japan by Yamaishi et al. (1998) calculated the groundwater discharge by assuming that the permeability values of rock tanks (i.e., empty spaces) were equal to infinity in the numerical model. In both of these previous studies, the groundwater was discharged outside the numerical model domain and excluded from the numerical calculation after discharge. This was a reasonable assumption because groundwater percolating into the excavated areas was pumped up to the ground surface in both the Kamaishi mine and underground oil storage facility.

However, such an assumption for large, empty underground spaces in numerical modeling is not applicable to the excavated areas of many metal sulfide underground mines, because these spaces are often back-filled with sand slime, tailings, and

97 sludge/precipitates formed by neutralization, which means these are no longer empty
98 spaces. Tomiyama et al. (2019) showed that AMD formed in the old mine workings
99 (i.e., drift and shaft) of a closed mine flowed through and interacted with the back-filled
100 materials into the empty spaces, and that the geochemical properties of AMD fluids
101 were dramatically changed. Based on this previous study, it is probably more
102 appropriate to consider old mine workings as porous media where water flow is
103 governed by Darcy's law rather than as free discharging boundaries.
104 In this study, we evaluated the assumption that back-filled excavated areas of old
105 mine workings can be modeled as porous media, where groundwater flow is governed
106 by Darcy's law. The site selected for this study was the Yatani mine, which is a closed
107 underground mine located in Yamagata Prefecture, Japan, where several different
108 mining methods were adopted and detailed drawings of the excavated areas are
109 available. A numerical model was constructed based on the topography of the mine and
110 mining methods, as well as the geological and hydrological properties of the site. The
111 model calibration was based on hydraulic conductivities (k) of volcanic rocks and faults.
112 In addition, we compared and verified the results of the model with actual AMD fluxes
113 measured on-site, and we then used the verified model to evaluate possible
114 countermeasures to reduce AMD flux from the closed mine.
115
116 **2. Site description**
117 *2.1. Geology and history of the mine*
118 The Yatani mine is located 28 km southwest of Yonezawa City, within the Bandai–
119 Asahi National Park (Fig. 1). It is situated in the green tuff area of northeast Japan, and
120 comprises granitic basement overlain by Neogene volcanic and sedimentary rocks.

Surface mining began in 1870 after the discovery of gold (Au) ore outcrops. When these were exhausted, mining continued underground for several decades. Taihei Mining Co. Ltd. acquired mining rights to the area in 1952 and began mining Pb and Zn ores. By 1978, the monthly crude ore output was >10,000 tons with average Pb and Zn grades of 2.0% and 4.4%, respectively. Decreasing metal prices and the appreciated Japanese yen eventually made the operation unprofitable, and it was closed in 1988 (Sato et al., 1978).

The Yatani ore deposit is of hydrothermal origin, formed within green tuff host rock. It includes two types of veins: one rich in Pb and Zn, and the other containing Au and silver (Ag). The Pb–Zn ore deposits constitute the main veins of the mine, reaching a maximum width of ~10 m, and which closely follow NE–SW- and E–W-trending faults in the area. The Pb–Zn veins comprise mainly quartz, galena, sphalerite, and pyrite, and sometimes include native Au and argentite. The Au–Ag ore veins contain quartz, native Au, argentite, pyrite, and rhodochrosite. In both types of veins, the ore minerals exhibit banded textures, indicating that quartz crystallized first, followed by precipitation of galena and zincblende, and finally by deposition of native Au and argentite (Taniguchi, 1969).

Two mining methods were used at the mine, involving the cut and fill method in deeper parts using sand slime, sludge and precipitates, and tailings as filling materials, and the shrinkage stoping method in shallower parts (Fig. 2). A mineral concentration system with its own power substation and repair facilities was constructed underground. Old mine workings deeper than the drainage level (–2L level) are kept submerged and AMD is currently treated by neutralization.

145 *2.2. Hydrogeochemistry*

146 The old mine workings of the Yatani mine have been generating AMD. Tomiyama
147 et al. (2019) investigated the formation and geochemical evolution of AMD on-site and
148 found that AMD is being formed by the interaction of groundwater with sulfide
149 minerals, sand slime, and tailings back-filled into excavated mine areas (Fig. 3;
150 Tomiyama et al., 2019). Groundwater recharge areas were identified on the mountain
151 slope at an elevation of ~900 m. The formation of AMD in the drifts and shaft was more
152 extensive than that in the deeper drainage levels. Principal component analysis was
153 applied to the hydrogeochemical data to identify the causes of AMD formation. The
154 first, second, and third principal components revealed that the increased ion
155 concentrations in the mine drainage are the result of water–mineral reactions in
156 excavated mine areas, contribution of groundwater in deep reducing environments, and
157 isotopic fractionation during precipitation, respectively (Tomiyama et al., 2019).
158

159 **3. Materials and methods**

160 *3.1. Sample collection and analysis*

161 To identify sources of heavy metals and evaluate possible countermeasures to
162 reduce AMD flux, mine drainage samples were collected and analyzed on 1 August and
163 9 October 2007, on the same dates as the flux measurements, from the locations shown
164 in Fig. 4. Samples S-1 to S-10 were collected from prominent parts of the drainage
165 tunnel (–2L level) where significant discharge of groundwater was observed (e.g., from
166 cracks in drainage tunnel walls). Samples M-1 to M-5 were also collected from the five
167 points where AMD fluxes were measured. All samples were stored in 1 L
168 polypropylene bottles before filtering through 0.22 μm membrane filters. Temperature

169 and pH were measured on-site using a thermo-pH meter (KS-701; Shindengen Electric
170 Manufacturing, Japan), and electrical conductivity (EC) was measured on-site using an
171 EC meter (B-173; Horiba, Japan).
172 All sample analyses were performed at the Analytical Center of Mitsubishi
173 Materials Techno Corporation (Tokyo, Japan). Zn, total-Fe, total-Mn, Pb, and Cu were
174 analyzed by either inductively coupled plasma–mass spectrometry (ICP–MS; Agilent
175 7700X; Agilent Technologies Japan, Japan) or inductively coupled plasma–atomic
176 emission spectroscopy (ICP–AES; ICAP-575; Thermo Fisher Scientific K.K., Japan).
177
178 *3.2. Numerical simulation*
179 *3.2.1. Calculation method*
180 Modeling of the Yatani mine assumed that the mined area above the drainage tunnel
181 (–2L level), which is located near the middle of the mining area, was an unsaturated
182 zone. Saturated–unsaturated groundwater flow analysis was applied to the groundwater
183 flow in the unsaturated zone (Table 1) using non-commercial Dtransu-3D-EL software
184 (Hishiya et al., 1999) together with G-TRAN/3D pre- and post-processing software for
185 Dtransu-3D (Geoscience Research Laboratory, Japan; Tomiyama et al., 2010a).
186 Dtransu-3D-EL software solves the equation for saturated–unsaturated groundwater
187 flow derived from mass conservation principles and Darcy's equation, which can be
188 written as follows:

189 $$\rho_f \theta \gamma \frac{\partial c}{\partial t} + \rho\{\beta Ss + Cs(\theta)\}\frac{\partial \varphi}{\partial t} = \frac{\partial}{\partial x_i}\left\{\rho K^S{}_{ij} K_r(\theta)\frac{\partial \varphi}{\partial x_i} + \rho K^S{}_{i\beta} K_r(\theta)\rho_r\right\} \quad (1)$$

190 where φ is the pressure head (L), θ is the volumetric water content (-), t is time (T), Ss is
191 the specific storage (L^{-1}), $Cs(\theta)$ is the specific moisture capacity (L^{-1}), $K^S{}_{ij}$ is the
192 directional components of the unsaturated hydraulic conductivity function ($L\ T^{-1}$), $K_r(\theta)$

193 is the relative hydraulic conductivity (-), ρ_f is the solvent density (M L^{-3}), ρ is the fluid
194 density (M L^{-3}), ρ_r is the ratio of ρ_f to ρ (-), $\beta = 1$ is the saturated zone, $\beta = 0$ is the
195 unsaturated zone, and γ is the solute density ratio (Hishiya et al., 1999). The source code
196 of Dtransu-3D-EL software is publicly available (Okayama University, 2019). This
197 source code has been used in previous studies for research into geological disposal of
198 high-level radioactive waste, unsaturated zone water flow within excavated mine sites,
199 and groundwater flow within the sediments of coastal plains (e.g., Kurikami et al.,
200 2008; Yamaguchi et al., 2015; Takamoto et al., 2017). In order to predict and analyze
201 seasonal variations of the AMD fluxes, two seasons of the year in which the AMD flux
202 increased (i.e., high rainfall days) and decreased (i.e., low rainfall days) were selected
203 for the model calibration. Results of the numerical simulation of groundwater flow were
204 verified on 1 August and 9 October 2007, by measuring the AMD flux at five different
205 points along the drainage tunnel (Fig. 5). Steady state analysis of groundwater flow was
206 performed using these actual measurements as boundary conditions of infiltration down
207 from the ground surface.
208
209 *3.2.2. Model set-up and calibration*
210 The model domain has an area of 33 km^2, an elevation range of 2.0 km, and is
211 bounded by a topographic ridge, below which the excavated areas and drainage tunnel
212 are located (Fig. 6a). The topography was reproduced in the numerical simulation using
213 a digital elevation model (DEM) created based on digital maps published by the
214 Geospatial Information Authority of Japan (Geospatial Information Authority of Japan,
215 2018). The distribution of each stratum and fault was based on the detailed geological
216 maps of Sato et al. (1978) and Taniguchi (1969). The excavated areas were classified

217 into shrinkage stoping, cut and fill with tailings, and cut and fill with sand slime, based
218 on records of the mining operations (Fig. 2). The element size was set to x = 50 m and z
219 = 50 m, with thicknesses of 1 to 500 m. The drainage tunnel was modeled with an actual
220 height of 2 m, width of 2 m, and length of 2,250 m. The vertical shaft and drifts were
221 then put together within the excavated areas. The size of the mining area was 1050 m in
222 the E–W direction and 600 m deep, with an assumed thickness of 2 m.
223 The hydraulic conductivities of volcanic rocks and faults in the mine area were
224 adjusted within allowable ranges for the trial-and-error calibration, which involved
225 combinations of *k* values, with the best-matched cases being selected by comparing
226 calculated and measured AMD fluxes. The hydraulic conductivities (*k*) and unsaturated
227 properties of numerical blocks representing surface soil, volcanic rocks, granitic rocks,
228 and dikes and faults, as well as the excavated areas were based on either *in situ*
229 measured values or estimated from the results of previous studies (Table 2; Fig. 6b).
230 Hydraulic conductivities (*k*) were calculated from water injection test results conducted
231 during a deep borehole survey in the northern part of Azuma, located just 10 km east of
232 the Yatani mine (New Energy and Industrial Technology Development Organization,
233 1987), and surface soil permeability data collected throughout Japan (Umeda et al.,
234 1995). Neogene volcanic rocks that are the host rocks of the deposit at the mine have a
235 wide range of hydraulic conductivities (*k*). For this reason, the model was calibrated
236 using each possible value. There are E–W- and NE–SW-trending faults in the mine
237 area, which are potential groundwater flow paths. Considering the heterogeneity of the
238 strata, incorporating the faults into the model is important. However, the permeability of
239 faults at the Yatani mine site and in nearby areas is unknown, so the sensitivity analysis
240 was performed with reference to actual measurements from another mine study

241 (Tomiyama et al., 2010b), in conjunction with the permeability values of the volcanic
242 rocks (Table 3). Hydraulic conductivity (k) values of the excavated areas were based on
243 previous studies (Fala et al., 2005; Tomiyama et al., 2010b; Ethier et al., 2018).
244 Shrinkage stoping was considered anisotropic with a horizontal/vertical saturated
245 hydraulic conductivity ratio (k_h/k_v) of 10^{-6}, based on a previous study related to
246 hydrogeology of several mine sites in Japan (Kondo, 1958).
247 The properties of the various geological strata under unsaturated conditions were
248 consistent with the moisture characteristic curve and saturated versus unsaturated
249 hydraulic conductivity coefficients of the van Genuchten (1980) model, which are given
250 by

251 $$s_e(\varphi) = \frac{\theta - \theta_r}{\theta_s - \theta_r} = \left[\frac{1}{1 + |a\varphi|^n}\right]^m \quad (2)$$

252 $$k_r\{s_e(\varphi)\} = {s_e}^l \left[1 - \left(1 - {s_e}^{1/m}\right)^m\right]^2 \quad (3)$$

253 where S_e is the effective water saturation (-), φ is the pressure head (L), θ is the
254 volumetric water content (-), θ_s is the saturated water content (-), θ_r is the residual water
255 content (-), a is the van Genuchten (1980) parameter (L^{-1}), m and n are the van
256 Genuchten (1980) parameters (-), kr is the relative hydraulic conductivity (-), and l is a
257 parameter representing the degree of pore connectivity (-). The van Genuchten
258 parameters used for the current simulations are presented in Table 4, and the
259 corresponding curves are shown in Fig. 7. In the hydraulic conductivity curves, the
260 minimum unsaturated hydraulic conductivity was set at 10^{-14} m s^{-1} (Pabst et al., 2018).
261
262 *3.2.3. Boundary conditions*
263 The boundary conditions of the numerical simulations were as follows: i. the river
264 was assumed to be connected to the groundwater surface and was set with a fixed head

boundary condition (pressure head = 0 m); ii. the ground surface (except that of the river) was set as an infiltration boundary condition (Table 1). The infiltration rate was calculated from the water balance of the surface basin as follows:

$$P = R + E + I \quad (4)$$

where P (mm d^{-1}) is precipitation, R (mm d^{-1}) is runoff, E (mm d^{-1}) is evapotranspiration, and I is infiltration (groundwater recharge). Precipitation values were based on measurements from a monitoring station in the mine area (Fig. 1), and runoff values were taken from the river water flux data of Mogami River (Ministry of Land, Infrastructure, Transport and Tourism, 2008). Evapotranspiration values were calculated following Takahashi (1979).

Water mass-balance values for each month are shown in Fig. 8. The values for runoff were an annual average of 3.5 mm d^{-1} (runoff rate = 0.57), and the estimated infiltration for each month was 0 to 3.4 mm d^{-1}. The relationship between measured AMD flux and estimated average infiltration for the preceding three months has a high degree of correlation (Fig. 9). Therefore, the average recharge volume of rainwater was calculated from the estimated infiltration in the three months immediately prior to the actual measurement date of the AMD flux (high rainfall days = May 1 to July 31, 2007; low rainfall days = July 9 to October 8, 2007). The average of infiltration rate was 1.2 mm d^{-1} during the high rainfall days (recharge rate = 0.08) and 0.42 mm d^{-1} during the low rainfall days (recharge rate = 0.03). Steady-state analysis of groundwater flow was performed using these infiltration rates during high- and low-rainfall days as boundary conditions for infiltration from the ground surface.

287 Both the drainage tunnel and vertical shaft were set to seepage boundary conditions,
288 which were incorporated into the numerical model by setting the total head value from
289 636 to 644 m at designated positions.
290
291 **4. Results and discussion**
292 *4.1. Contaminants in the water samples*
293 The geochemical properties of water samples collected from the drainage tunnel are
294 summarized in Table 5, and spatial variations in pH and EC are shown in Fig. 10. The
295 pH, EC, and temperature of the seepage water samples were in the ranges of 6.72–7.31,
296 21.5–91.1 mS m^{-1}, and 11.6°C–17.4°C (1 August 2007), and 6.64–7.37, 21.5–108.6 mS
297 m^{-1}, and 12.1°C–17.5°C (9 October 2007), respectively. Sample S-1 had the highest pH
298 and lowest EC. The sampling site of S-1 was at a NE–SW-trending fault (Sato et al.,
299 1978), and the water was emanating from fractures in the wall rocks (Fig. 4). This
300 suggests that sample S-1 may be river water that has infiltrated the drainage tunnel
301 through the fault.
302 The pH, EC, and temperature of the mine drainage samples were in the ranges of
303 5.12–6.37, 100.1–178.3 mS m^{-1}, and 15.9°C–18.9°C (1 August 2007), and 5.27–6.53,
304 104.3–141.9 mS m^{-1}, and 16.0°C–19.3°C (9 October 2007), respectively. EC, pH, and
305 concentrations of heavy metals vary with location. EC values and concentrations of
306 heavy metals increase with decreasing pH from the adit mouth to veins and shaft (Fig.
307 10). Drainage sample M-5 from the drift has the highest EC (178.2 mS m^{-1}) and lowest
308 pH (5.12). A similar trend was observed for concentrations of heavy metals in the mine
309 drainage samples. Zn, total-Fe, and total-Mn concentrations in samples collected at the
310 adit mouth (sample M-1) were ~20, ~30, and ~40 mg L^{-1}, respectively, while those

311 from near veins, the drift, and the shaft (sample M-5) were ~2 times higher,
312 respectively. Fluxes of heavy metals (Zn, T-Fe, T-Mn, and Pb) in the drainage water are
313 shown in Fig. 4. The actual mine drainage was measured at the same locations as the
314 drainage water sampling sites, and the element flux values were calculated by
315 multiplying the element concentrations by the volume discharge of mine drainage. For
316 example, in the case of Zn, the fluxes at the adit mouth (point M-1) were 58.1 and 37.7
317 g min^{-1} during the high and low rainfall days, respectively, which were 1.4 and 1.8
318 times higher than the Zn flux around the shaft and drift (point M-5; 2200 m from the
319 adit mouth). The other heavy metals (T-Fe, T-Mn, and Pb) display the same trend, and
320 60%–80% of the heavy metals in AMD from the wellhead are generated from the
321 vertical shaft and drifts (i.e., the excavated areas). However, water was sampled only
322 twice, on 1 August and 9 October 2007. The total AMD flux measured at the
323 neutralization treatment plant increased during the snowmelt season of March–May
324 2008, with pH decreasing over that time (Fig. 5). This suggests that the groundwater
325 flux, infiltrating from the mountain slope to the excavated area and reacting with sulfide
326 minerals, increased during the snowmelt season (Tomiyama et al., 2019). Therefore,
327 when the total AMD flux increases and pH decreases in the snowmelt season, 60%–
328 80% of the heavy metals in AMD from the adit mouth may be generated from the
329 vertical shaft and drifts.
330
331 *4.2. Model calibration*
332 Table 6 and Fig. 11 compare the modeled total AMD fluxes by groundwater flow
333 analysis with those measured on-site. The calculated AMD flux strongly depends on the
334 permeability of the Neogene volcanic rocks and faults. The AMD flux was highest in

335 Case D-4 where Neogene volcanic rocks ($k = 2.1 \times 10^{-7}$ m s^{-1}) and faults (k = 1×10^{-4}
336 m s^{-1}) have higher permeability, and lowest in Case A-1, where it is assumed that the
337 Neogene volcanic rocks ($k = 3.3 \times 10^{-9}$ m s^{-1}) and faults ($k = 1 \times 10^{-7}$ m s^{-1}) have lower
338 permeability. The results for cases where hydraulic conductivities (k) of rock and faults
339 were 3.5×10^{-8} m s^{-1} and 1.0×10^{-5} m s^{-1}, respectively, (3.52 m^3 min^{-1} during high
340 rainfall days and 2.67 m^3 min^{-1} during low rainfall days) were the closest to the
341 measured total AMD flux (3.47 m^3 min^{-1} and 2.62 m^3 min^{-1}, respectively).
342
343 *4.3. Model verification*
344 Variations in water flux along the mine drainage were also evaluated by numerical
345 modeling and compared with those measured on-site. Figure 12 shows the relationship
346 between the AMD fluxes predicted by the numerical model and those measured on-site
347 for the cases where rock and faults hydraulic conductivities are 3.5×10^{-8} m s^{-1} and 1.0
348 $\times 10^{-5}$ m s^{-1}, respectively. The actual AMD flux were measured at the adit mouth and in
349 four locations along the drainage tunnel (–2L level) from the adit mouth at 780, 1255,
350 1712, and 2200 m. The total AMD flux measured on-site gradually increased as AMD
351 flowed through the drainage tunnel towards the adit mouth. The measured AMD fluxes
352 around the shaft and drifts (2200 m from the adit mouth) were 1.14 and 0.77 m^3 min^{-1}
353 during the high and low rainfall days, respectively, which accounted for 29–33% of the
354 total AMD flux. In comparison, the modeled AMD flux at the same locations were 1.20
355 and 0.84 m^3 min^{-1} during the high and low rainfall days, respectively, and accounted for
356 31%–34% of the total AMD flux. These results show that the numerical model
357 successfully predicted not only the AMD fluxes at various locations along the drainage
358 tunnel, but also the contributions of various locations along the drainage tunnel to the

359 total AMD flux. Moreover, the numerical model correctly predicted the increasing trend
360 of total AMD flux towards the adit mouth, when taking into account the presence of
361 faults and its permeability. Fig. 13 shows a cross-section of the total water head
362 distribution along the drainage tunnel (–2L level) during high-rainfall days. The
363 numerical model predicted that the groundwater flowing into the shaft originated from
364 the unsaturated zone just above the excavated area, while the groundwater flowing into
365 the excavated area comes from the hill slope north of the old mine workings. The
366 modeling indicates that a faster groundwater flow (max Darcy flow velocity = 30 m d^{-1})
367 was obtained in the upper excavated area around the shaft than in the surrounding areas,
368 which then flowed down into the areas mined using shrinkage stoping. In the drainage
369 tunnel, significant discharge of groundwater was observed from the top part of the shaft,
370 supporting the model results. These results suggest the presence of preferential
371 groundwater flow areas within the old mine workings of the Yatani mine, and are
372 consistent with 60%–80% of the heavy metals in the AMD being generated from the
373 excavated areas. In the region from the hill slope on the north side to the lower part of
374 the excavated area, regions with Darcy flow velocities between 0.01 and 0.1 m d^{-1} were
375 widely distributed and groundwater flow in the saturation zone was also predicted.
376 Groundwater flow below the old mine workings predicted by the numerical model most
377 likely corresponds to the lower groundwater flow shown in Fig. 3. Based on these
378 results, groundwater and/or AMD flow in back-filled old mine workings in underground
379 mines could be modeled as porous media governed by Darcy's law.
380
381 *4.4. Reduction of the AMD flux*

382 In the Yatani mine, AMD is currently neutralized by the addition of calcium oxide
383 that removes most of the heavy metals, and the treated water is discharged into a nearby
384 river. One possible way to lower the cost of AMD treatment is to reduce the AMD flux.
385 This could be achieved by back-filling the excavated areas with low permeability
386 materials (e.g., a mixture of cement and sludge–precipitate or cemented paste). Using
387 the calibrated numerical model, the applicability of this approach was tested by
388 assuming that the shrinkage stoping areas were filled with a low permeability material
389 ($k < 10^{-8}$ m s^{-1}; i.e., 10^{-9} m s^{-1}). The numerical model predicts that, under these
390 conditions, the total AMD flux decreases to 2.24 and 1.72 m^3 min^{-1} during high and low
391 rainfall days, respectively. Most of the decrease in total AMD flux was due to the
392 decrease in AMD fluxes around the shaft and drifts, and the decreases with respect to
393 the measured values of 1.14 and 0.77 m^3 min^{-1} (during the high and low rainfall days,
394 respectively) are 84% and 82%, respectively. In this case, taking Zn as an example, it is
395 estimated that the total AMD Zn flux will be reduced by 61% and 48% during high- and
396 low-rainfall days, respectively.
397 Figure 14b shows cross-sections of the groundwater flow vectors around the mining
398 area, and Fig. 14c shows the result when assuming the shrinkage stoping areas were
399 infilled (for high rainfall days). In Fig. 14b, the groundwater flow infiltrating from the
400 periphery of the excavated areas through the faults was reproduced. However, Fig. 14c
401 indicates that the infiltration of groundwater is suppressed by infilling the excavated
402 areas and the Darcy flow velocity becomes slow. Therefore, filling of the excavated
403 areas with low-permeability materials may be effective in limiting the formation of
404 AMD and the flux of heavy metals in the Yatani mine.
405

5. Conclusions

Groundwater flow patterns in the Yatani mine area located in Yamagata Prefecture, Japan, were elucidated using a numerical model. The model was constructed based on the topography around the mine, detailed geological maps of the area, and measured and/or estimated hydrological properties of the various deposits and geological strata under saturated–unsaturated conditions. The model calibration was performed using hydraulic conductivities of volcanic rocks and faults, with the best-matched case being selected by comparing calculated AMD and measured AMD fluxes. In addition, the numerical model was verified using actual AMD fluxes measured on-site in order to evaluate possible countermeasures for the reduction of AMD flux. The modeled AMD fluxes along the drainage tunnel (–2L level) agreed with the measured data, when the excavated areas were considered to be porous media with a specific hydraulic conductivity and the presence of faults and permeability were taken into account. Back-filling old underground mines was shown to be a potentially useful countermeasure to reduce AMD flux. The model results indicate that the flux of Zn in AMD could be reduced by up to 61% if the excavated areas are back-filled with low permeability materials, regardless of the rainfall intensity. The approach used in this study is applicable to vein-type deposits that are mined in the same way as the Yatani mine. The assessed AMD reduction was similar to that of other studies (e.g., Yamaguchi et al., 2015). It is possible that a trace of oxygen may oxidize pyrite to sulfate, making it difficult to prevent acidification (Yamaguchi et al., 2015). Furthermore, we only modeled an area over several kilometers and geochemical data were not integrated into the model. When cement-based materials are used for infilling, changes in water quality due to oxygen suppression and neutralization reactions are expected. Recent studies

have examined chemical transfer processes in waste rock piles (e.g., Lahmira et al., 2016; Ethier et al., 2018), and chemical modeling is the next step in improving our understanding of such large-scale mining areas.

Acknowledgements

The authors thank the editor and anonymous reviewers for their constructive comments that improved this manuscript. The authors thank the staff of Mitsubishi Materials Corporation, Eco-Management Corporation, and Mitsubishi Materials Techno Corporation for their help, advice, and cooperation during this study.

Funding: This research did not receive any specific grant from funding agencies in the public, commercial, or not-for-profit sectors.

REFERENCES

Anawar, H.M, 2015. Sustainable rehabilitation of mining waste and acid mine drainage using geochemistry, mine type, mineralogy, texture, ore extraction and climate knowledge. J. Environ. Manag. 158, 111–121.

Andrea, I.S., Sanz, J.L., Bijmans, M.F.M, Stams, A.J.M., 2014. Sulfate reduction at low pH to remediate acid mine drainage. J. Hazard. Mater. 269, 98–109.

Bahrami, S., Ardejani, F.D., Baafi, E., 2016. Application of artificial neural network coupled with genetic algorithm and simulated annealing to solve groundwater inflow problem to an advancing open pit mine. J. Hydrol. 536, 471–487.

452 Bain, J.G., Blowes, D.W., Robertson, W.D., Frind, E.O., 2000. Modelling of sulfide
453 oxidation with reactive transport at a mine drainage site. J. Contam. Hydrol. 41, 23–
454 47.
455 Boularbah, A., Schwartz, C., Bitton, G., Morel, J.L., 2006. Heavy metal contamination
456 from mining sites in South Morocco: I. Use of a biotest to assess metal toxicity of
457 tailings and soils. Chemosphere 63, 802–810.
458 Bussière, B., Aubertin, M., Chapuis, R.P., 2003. The behavior of inclined covers used
459 as oxygen barriers. Can. Geotech. J. 40, 512–535.
460 Cánovas, C.R., Macías, F., Olías, M., Pérez López, R., Nieto, J.M., 2017. Metal-fluxes
461 characterization at a catchment scale: Study of mixing processes and end-member
462 analysis in the Meca River watershed (SW Spain). J. Hydrol. 550, 590–602.
463 Castendyk, D.N., Webster-Brown, J.G., 2007. Sensitivity analyses in pit lake prediction,
464 Martha mine, New Zealand 2: Geochemistry, water–rock reactions, and surface
465 adsorption. Chem. Geol. 244, 56–73.
466 Ethier, M.P, Bussière, B., Broda, S., Aubertin, M., 2018. Three-dimensional
467 hydrogeological modeling to assess the elevated-water-table technique for
468 controlling acid generation from an abandoned tailings site in Quebec, Canada.
469 Hydrogeol. J. 26, 1201–1219.
470 Fala, O., Molson, J., Aubertin, M., Bussière, B., 2005. Numerical modelling of flow and
471 capillary barrier effects in unsaturated waste rock piles. Mine Water Environ. 24,
472 172–185.
473 Galván, L., Olías, M., Cánovas, C.R., Sarmiento, A.M., Nieto, J.M., 2016. Hydrological
474 modeling of a watershed affected by acid mine drainage (Odiel River, SW Spain).
475 Assessment of the pollutant contributing areas. J. Hydrol. 540, 196–206.

476 Gammons, C.H., Duaime, T.E., Parker, S.R., Poulson, S.R., Kennelly, P., 2010.
477 Geochemistry and stable isotope investigation of acid mine drainage associated with
478 abandoned coal mines in central Montana, USA. Chem. Geol. 269, 100–112.
479 Gault, A.G., Cooke, D.R., Townsend, A.T., Charnock, J.M., Polya, D.A., 2005.
480 Mechanisms of arsenic attenuation in acid mine drainage from Mount Bischoff,
481 western Tasmania. Sci. Total Environ. 345, 219–228.
482 Geospatial Information Authority of Japan (GSI), 2018. Geospatial Information
483 Authority of Japan Website, http://www.gsi.go.jp/ENGLISH/page_e30286.html.
484 Hazen, J.M., Williams, M.W., Stover, B., Wireman, M., 2002. Characterisation of acid
485 mine drainage using a combination of hydrometric, chemical and isotopic analyses,
486 Mary Murphy Mine, Colorado. Environ. Geochem. Health, 24, 1–22.
487 Hien, N.T.T., Yoneda, M., Matsui, A., Hai, H.T., Pho, N.V., Quang, N.H., 2012.
488 Environmental contamination of arsenic and heavy metals around Cho Dien lead
489 and zinc mine, Vietnam. J. Water Environ. Technol. 10, 253–265.
490 Hierro, A., Olías, M., Cánovas, C.R., Martín, J.E., Bolivar, J.P., 2014. Trace metal
491 partitioning over a tidal cycle in an estuary affected by acid mine drainage (Tinto
492 estuary, SW Spain). Sci. Total Environ. 18–28, 497–498.
493 Hishiya, T., Nishigaki, M., Hashimoto, N., 1999. The three dimensional numerical
494 analysis method for density dependent groundwater flow with mass transport. J.
495 Constr. Man. Eng. 638, 59–69.
496 Hubbard, C.G, Black, S., Coleman, L., 2009. Aqueous geochemistry and oxygen
497 isotope compositions of acid mine drainage from the Río Tinto, SW Spain, highlight
498 inconsistencies in current models. Chem. Geol. 265, 321–334.

499 Iakovleva, E., Mäkilä, E., Salonen, J., Sitarz, M., Wang, S., Sillanpää, M., 2015. Acid
500 mine drainage (AMD) treatment: Neutralization and toxic element removal with
501 unmodified and modified limestone. Ecol. Eng. 81, 30–40.
502 Imai, H., Amemiya, K., Matsui, H., Sato, T., Saegusa, H., Watanabe, K., 2013. The
503 proposal relevant to seepage flow simulation in rockmass around tunnel under
504 unsaturated condition—method for estimating unsaturated seepage parameters of
505 stones and setting of boundary condition on tunnel wall. Journal of JSCE C69, 285–
506 296 (in Japanese with English abstract).
507 Iwatsuki, T., Yoshida, H., 1999. Groundwater chemistry and fracture mineralogy in the
508 basement granitic rock in the Tono uranium mine area, Gifu Prefecture, Japan:
509 Groundwater composition, Eh evolution analysis by fracture filling minerals.
510 Geochem. J. 33, 19–32.
511 Japan Nuclear Cycle Development Institute, 1999. Final report of Kamaishi *In-situ*
512 experiment, JNC TN7410 99-001, pp. 1–80.
513 Kazama, S., Tada, T., Sawada, M., 1996. Analysis of yearly water balance in the
514 Tohoku district using satellite data. Annual Journal of Hydraulic Engineering, JSCE,
515 40, 81–86 (in Japanese with English abstract).
516 Kimball, B.A., Walton-Day, K., Runkel, R.L., 2007. Quantification of metal loading by
517 tracer injection and synoptic sampling, 1996–2000, in Church, S.E., von Guerard,
518 P., Finger, S.E. (Eds.), Integrated Investigations of Environmental Effects of
519 Historical Mining in the Animas River Watershed, San Juan County, Colorado. U.S.
520 Geological Survey Professional Paper 1651, 417–495.
521 Kondo, S., 1958. On fissures and percolation of water in rock formations. Bulletin of
522 the Geological Survey of Japan, 9, 67–76 (in Japanese with English abstract).

523 Kurikami, H., Takeuchi, R., Yabuuchi, S., Seno, S., Tomura, G., Shibano, K., Hara, M.,
524 Kunimaru, T., 2008. Hydrogeological investigations of surface-based investigation
525 phase of Horonobe URL project. Journal of JSCE C 64, 680–695 (in Japanese with
526 English abstract).
527 Lahmira, B., Lefebvre, R., Michel Aubertin, M., Bussière B., 2016. Effect of
528 heterogeneity and anisotropy related to the construction method on transfer
529 processes in waste rock piles. J. Contam. Hydrol. 184, 35–49.
530 Lee, J.S., Chon, H.T., 2006. Hydrogeochemical characteristics of acid mine drainage in
531 the vicinity of an abandoned mine, Daduk Creek, Korea. J. Geochem. Explor. 88,
532 37–40.
533 Leybourne, M.L., Clark, I.D., Goodfellow, W.D., 2006. Stable isotope geochemistry of
534 ground and surface waters associated with undisturbed massive sulfide deposits;
535 constraints on origin of waters and water–rock reactions. Chem. Geol. 231, 300–
536 325.
537 Li, X., Hiroyoshi, N., Tabelin, C.B., Naruwa, K., Harada, C., Ito, M., 2019. Suppressive
538 effects of ferric–catecholate complexes on pyrite oxidation. Chemosphere 214, 70–
539 78.
540 Lim, H.S., Lee, J.S., Chon, H.T., Sager, M., 2008. Heavy metal contamination and
541 health risk assessment in the vicinity of the abandoned Songcheon Au–Ag mine in
542 Korea. J. Geochem. Explor. 96, 223–230.
543 Mahara, Y., Nakata, E., Ooyama, T., Miyakawa, K., Igarashi, T., Ichihara, Y.,
544 Matsumoto, K., 2006. Proposal for the methods to characterize fossil seawater:
545 Distribution of anions, cations and stable isotopes, and estimation on the

546 groundwater residence time by measuring ^{36}Cl at the Taiheiyou Coal Mine. J.
547 Groundwater Hyd. 48, 17–33 (in Japanese with English abstract).
548 Migaszewski, Z.M., Gałuszka, A., Dołęgowska, S., 2018. Arsenic in the Wiśniówka
549 acid mine drainage area (south–central Poland) – Mineralogy, hydrogeochemistry,
550 remediation. Chem. Geol. 493, 491–503.
551 Ministry of Land, Infrastructure, Transport and Tourism (MLIT), 2008. Hydrological
552 water quality database website: http://www1.river.go.jp/contents.html. Accessed 27
553 September 2019.
554 Molson, J.W., Fala, O., Aubertin, M., Bussière, B., 2005. Numerical simulations of
555 pyrite oxidation and acid mine drainage in unsaturated waste rock piles. J. Contam.
556 Hydrol. 78, 343–371.
557 New Energy and Industrial Technology Development Organization (NEDO), 1987.
558 Azumahokubu. Chinetsu-kaihatsu-sokushin-chosa-houkokusho, No. 10, 539–550 (in
559 Japanese).
560 Okayama University, 2019. Department of Environmental and Civil Design, Faculty of
561 Environmental Science and Technology website: http://gw.civil.okayama-
562 u.ac.jp/gel_home/download/. Accessed 27 September 2019.
563 Okumura, M., 2003. Hydrogeochemical study of the 3M level adit drainage at the old
564 Matsuo mine. Resources Geol. 53, 173–182 (in Japanese with English abstract).
565 Pabst, T., Bussière, B., Aubertina, M., Molson, J., 2018. Comparative performance of
566 cover systems to prevent acid mine drainage from pre-oxidized tailings: A
567 numerical hydro-geochemical assessment. J. Contam. Hydrol. 214, 39–53.

568 Park, I., Tabelin, C.B., Magaribuchi, K., Seno, K., Ito, M., Hiroyoshi, N., 2018a.
569 Suppression of the release of arsenic from arsenopyrite by carrier–
570 microencapsulation using Ti-catechol complex. J. Hazard. Mater. 344, 322–332.
571 Park, I., Tabelin, C.B., Seno, K., Jeon, S., Ito M., Hiroyoshi, N., 2018b. Simultaneous
572 suppression of acid mine drainage formation and arsenic release by carrier–
573 microencapsulation using aluminumcatecholate complexes. Chemosphere 205, 414–
574 425.
575 Ramasamy, M., Power, C., Mkandawire, M., 2018. Numerical prediction of the long-
576 term evolution of acid mine drainage at a waste rock pile site remediated with an
577 HDPE-lined cover system. J. Contam. Hydrol. 216, 10–26.
578 Razowska, L., 2001. Changes of groundwater chemistry caused by the flooding of iron
579 mines (Czestochowa Region, southern Poland). J. Hydrol. 244, 17–32.
580 Sato, N., Takatori, I., Yanagisawa, S., 1978. Geology and ore deposits of the Yatani
581 Mine, Yamagata Prefecture, Japan, with special reference to some suggestions on
582 exploration. Mining Geol. 28, 177–190 (in Japanese with English abstract).
583 Satur, J., Hiroyoshi, N., Tsunekawa, M., Ito, M., Okamoto, H., 2007. Carrier–
584 microencapsulation for preventing pyrite oxidation. Int. J. Miner. Process. 83, 116–
585 124.
586 Skierszkan, E.K., Mayer, K.U., Weis, D., Beckie, R.D., 2016. Molybdenum and zinc
587 stable isotope variation in mining waste rock drainage and waste rock at the
588 Antamina mine, Peru. Sci. Total Environ. 550, 103–113.
589 Sracek, O., Choquette, M., Gélinas, P., Lefebvre, R., Nicholson, R.V., 2004.
590 Geochemical characterization of acid mine drainage from a waste rock pile, Mine
591 Doyon, Quebec, Canada. J. Contam. Hydrol. 69, 45–71.

592 Tabelin, C.B., Igarashi, T., 2009. Mechanisms of arsenic and lead release from
593 hydrothermally altered rock. J. Hazard. Mater. 169, 980–990.
594 Tabelin, C.B, Igarashi, T., Tamoto, S., Takahashi, R., 2012a. The roles of pyrite and
595 calcite in the mobilization of arsenic and lead from hydrothermally altered rocks
596 excavated in Hokkaido, Japan. J. Geochem. Explor. 119, 17–31.
597 Tabelin, C.B., Basri, A.H.M., Igarashi, T., Yoneda, T., 2012b. Removal of arsenic,
598 boron, and selenium from excavated rocks by consecutive washing. Water Air Soil
599 Pollut. 223, 4153–4167.
600 Tabelin, C.B., Igarashi, T., Yoneda, T., Tamamura, S., 2013. Utilization of natural and
601 artificial adsorbents in the mitigation of arsenic leached from hydrothermally altered
602 rock. Eng. Geol. 156, 58–67.
603 Tabelin, C.B., Veerawattananun, S., Ito, M., Hiroyoshi, N., Igarashi, T., 2017a. Pyrite
604 oxidation in the presence of hematite and alumina: I. Batch leaching experiments
605 and kinetic modeling calculations. Sci. Total Environ. 580, 687–698.
606 Tabelin, C.B., Veerawattananun, S., Ito, M., Hiroyoshi, N., Igarashi, T., 2017b. Pyrite
607 oxidation in the presence of hematite and alumina: II. Effects on the cathodic and
608 anodic half-cell reactions. Sci. Total Environ. 581–582, 126–135.
609 Tabelin, C.B., Li, X., Seng, S., Kojima, M., Igarashi, T., Ito, M., Hiroyoshi, N., 2017c.
610 Enhanced passivation of pyrite in phosphate solution using ferric–catechol complex
611 and zero-valent iron. In: Proceedings of the 14th International Symposium on East
612 Asian Resources Recycling Technology and the Mining and Materials Processing
613 Institute of Japan Fall Meeting, Sapporo, Japan, Special Session on Post Mining, pp.
614 8–13.

615 Tabelin, C.B., Igarashi, T., Villacorte-Tabelin, M., Park, I., Opiso, E.M., Ito, M.,
616 Hiroyoshi, N., 2018. Arsenic, selenium, boron, lead, cadmium, copper, and zinc in
617 naturally contaminated rocks: A review of their sources, modes of enrichment,
618 mechanisms of release, and mitigation strategies. Sci. Total Environ. 645, 1522–
619 1553.
620 Takahashi, K., 1979. Estimate of evapotranspiration based on monthly temperature and
621 precipitation. J. Meteor. Soc. Japan 26, 759–776 (in Japanese).
622 Takamoto, N., Shimada, J., Shiraishi, T., 2017. Reconstructing paleohydrological
623 conditions in Lake Kasumigaura during the Holocene using unsteady groundwater
624 flow simulation. J. Groundwater Hydrol. 59, 325–343 (in Japanese with English
625 abstract).
626 Taniguchi, H., 1969. Geology and ore deposits of the Yatani Mine, with special
627 reference to the gold and silver veins. Mining Geol. 19, 113–121 (in Japanese with
628 English abstract).
629 Tatsuhara, T., Arima, T., Igarashi, T., Tabelin, C.B., 2012. Combined neutralization–
630 adsorption system for the disposal of hydrothermally altered excavated rock
631 producing acidic leachate with hazardous elements. Eng. Geol. 139–140, 76–84.
632 Tomiyama, S., Ueda, A., Ii, H., Nakamura, Y., Koizumi, Y., Saito, K., 2010a. Sources
633 and flow system of groundwater in the Hosokura mine, Miyagi Prefecture, using
634 geochemical method and numerical simulation. J. MMIJ 126, 31–37 (in Japanese
635 with English abstract).
636 Tomiyama, S., Ii, H., Koizumi, Y., Metugi, H., 2010b. Modeling of groundwater
637 recharge and discharge in Tomitaka mine, Miyazaki Prefecture. J. Groundwater
638 Hydrol., 52, 261–274 (in Japanese with English abstract).

639 Tomiyama, S., Igarashi, T., Ii, H., Takano, H., 2016. Sources and flow system of
640 groundwater in the Shimokawa mine, north Hokkaido, using geochemical method
641 and numerical simulation. J. MMIJ 132, 80–88 (in Japanese with English abstract).
642 Tomiyama, S., Igarashi, T., Carlito, B.T., Tangviroon, P., Ii, H., 2019. Acid mine
643 drainage sources and hydrogeochemistry at the Yatani mine, Yamagata, Japan: A
644 geochemical and isotopic study. J. Contam. Hydrol. 225, 103502.
645 Tsutsumi, K., Watanabe, K., Suga, I., Yamawaki, S., 1994. Back analytical technique
646 for evaluating the hydraulic properties of unsaturated rock, J. Japan Soc. Eng. Geol.
647 35, 23–30 (in Japanese with English abstract).
648 Umeda, K., Yanagisawa, K., Yoneda, S., 1995. Creation of permeability coefficient
649 database for Japanese ground. J. Groundwater Hydrol. 37, 69–77 (in Japanese).
650 Van Genuchten, M.T., 1980. A closed-form equation for predicting the hydraulic
651 conductivity of unsaturated soils. Soil Sci. Soc. Am. J. 44, 892–898.
652 Wunsch, D.R., Dinger, J.S., Graham, D.R., 1999. Predicting ground-water movement in
653 large mine spoil areas in the Appalachian Plateau. Int. J. Coal Geol. 41, 73–106.
654 Yamaguchi, K., Tomiyama, S., Metugi, H., Ii, H., Ueda, A., 2015. Flow and
655 geochemical modeling of drainage from Tomitaka mine, Miyazaki, Japan. J.
656 Environ. Sci. 36, 130–143.
657 Yamaishi, T., Kobayashi, H., Tani, T., Okamoto, A., Tosaka, H., Kojima, K., 1998.
658 Complete numerical modeling and history matching of surface–subsurface–coupled
659 fluid behavior around underground oil storage plant. J. Groundwater Hydrol. 40,
660 167–183 (in Japanese with English abstract).
661 Younger, P.L., 2001. Mine water pollution in Scotland: Nature, extent and preventative
662 strategies. Sci. Total Environ. 265, 309–326.

663 Zhao, Q., Guo, F., Zhang, Y., Ma, S., Jia, X., Meng, W., 2017. How sulfate-rich mine
664 drainage affected aquatic ecosystem degradation in northeastern China, and
665 potential ecological risk. Sci. Total Environ. 609, 1093–1102.

Table 1. Basic configuration of the numerical model.

Boundary conditions	Side and bottom	Impermeable
	Ground surface	Infiltration: 1.2 mm d^{-1} (high rainfall days) 0.42 mm d^{-1} (low rainfall days)
	River	Pressure head: 0 m
	Drainage level and vertical shaft	Seepage (total head: 636–644 m)
Finite element method grid	Number of elements	79368
	Number of layers	8
	Basic element size	x = 50 m; y = 1–500 m; z = 50 m
Method of analysis	Saturated–unsaturated three-dimensional seepage analysis	

Table 2. Hydraulic conductivities and horizontal/vertical saturated hydraulic conductivity ratios (k_h/k_v) of geological strata and excavated areas. The fault has not been measured for permeability at the Yatani mine site or nearby, and the sensitivity analysis was performed with reference to actual measurements for the Tomitaka mine in Japan.

Type of geological strata and excavated area	Hydraulic conductivity k (m s^{-1})	k_h/k_v	Reference
Surface soil	9.2×10^{-6}	1	Umeda et al. (1995)
Neogene volcanic rocks	3.3×10^{-9}, 3.5×10^{-8}, 4.8×10^{-8}, 2.1×10^{-7}	1	NEDO (1987)
Granitic rocks and dikes	5.6×10^{-8}	1	NEDO (1987)
Faults	2.5×10^{-6}	1	Tomiyama et al. (2010b)
Shrinkage stoping	1.0×10^{-2}	10^{-6}	Tomiyama et al. (2010b)
Drainage tunnel	1.0×10^{-2}	1	Tomiyama et al. (2010b)
Cut and filled with tailings	7.0×10^{-7}	1	Ethier et al. (2018)
Cut and filled with sand slime	5.1×10^{-5}	1	Fala et al. (2005)

Table 3. Model calibration cases based on the hydraulic conductivity of Neogene volcanic rocks and faults.

Hydraulic conductivity k ($m\ s^{-1}$)		Neogene volcanic rocks			
		3.3×10^{-9}	3.5×10^{-8}	4.8×10^{-8}	2.1×10^{-7}
Faults	1.0×10^{-7}	Case A-1	Case B-1	Case C-1	Case D-1
	2.5×10^{-6}	Case A-2	Case B-2	Case C-2	Case D-2
	1.0×10^{-5}	Case A-3	Case B-3	Case C-3	Case D-3
	1.0×10^{-4}	Case A-4	Case B-4	Case C-4	Case D-4

Table 4. Residual water content θ_r, saturated water content θ_s, and van Genuchten (1980) parameters a, l, and n.

	θ_r(-)	θ_s(-)	a (m^{-1})	l(-)	n(-)	Reference
Tailings	0.00	0.42	0.15	0.5	1.87	Ethier et al. (2018)
Sand slime	0.01	0.29	3	0.5	3.72	Fala et al. (2005)
Granite	0.00	0.03	0.0001	0.15	2.26	Tutumi et al. (2013)
Andesite	0.00	0.104	0.06	0.5	3.57	Imai et al. (2013)

Table 5. Contaminant properties of the water samples.

Sample type	Collection date	Sample	Distance from adit mouth (m)	pH	EC (mS m^{-1})	Temp (°C)	Concentration (mg L^{-1})				
							Zn	Total-Fe	Total-Mn	Pb	Cu
Seepage water from the drainage tunnel wall	1 August 2007	S-1	703	6.72	21.5	12.0	<0.01	0.04	<0.01	<0.001	<0.01
		S-2	1,230	6.84	33.8	12.1	<0.01	0.03	0.44	<0.001	<0.01
		S-3	1,360	7.11	23.7	15.2	<0.01	0.02	0.12	<0.001	<0.01
		S-4	1,420	7.02	38.7	12.1	0.01	0.05	0.28	<0.001	<0.01
		S-5	1,555	7.12	45.1	11.6	0.29	1.6	4.2	0.002	<0.01
		S-6	1,704	7.23	36.8	17.1	<0.01	0.04	0.26	0.002	<0.01
		S-7	1,840	7.25	69.2	17.4	0.34	0.03	1.9	<0.001	<0.01
		S-8	1,910	7.31	91.1	17.4	<0.01	0.03	0.22	<0.001	<0.01
		S-9	1,985	7.20	36.5	14.8	<0.01	0.02	<0.01	<0.001	<0.01
		S-10	2,069	7.04	52.8	16.3	0.08	0.01	0.15	0.004	0.01
	9 October 2007	S-1	703	7.37	21.4	16.0	<0.01	0.03	<0.01	<0.001	<0.01
		S-2	1,230	7.00	33.7	12.1	<0.01	0.03	0.75	<0.001	<0.01
		S-3	1,360	6.79	21.5	15.2	<0.01	0.03	0.08	<0.001	<0.01
		S-4	1,420	7.05	38.8	11.8	<0.01	0.03	0.24	<0.001	<0.01
		S-5	1,555	6.85	44.3	11.4	0.29	1.5	3.7	0.001	<0.01
		S-6	1,704	6.64	36.6	17.0	<0.01	0.07	0.24	0.002	<0.01
		S-7	1,840	7.00	66.0	17.3	0.14	0.05	7.0	0.004	<0.01
		S-8	1,910	6.94	85.8	17.5	<0.01	<0.01	0.08	0.001	<0.01
		S-9	1,985	6.98	73.1	17.3	0.02	<0.01	1.5	<0.001	<0.01
		S-10	2,069	6.91	108.6	16.3	0.21	<0.01	1.1	0.002	<0.01
Mine drainage in the drainage tunnel	1 August 2007	M-1	0	6.37	100.1	15.9	24	32	37	0.12	0.01
		M-2	780	6.37	102.0	16.0	26	35	40	0.14	0.01
		M-3	1,255	6.22	134.2	17.9	38	51	56	0.20	0.02
		M-4	1,712	6.08	143.5	18.5	43	59	64	0.22	0.02
		M-5	2,200	5.12	178.2	18.9	51	75	76	0.30	0.02
	9 October 2007	M-1	0	6.53	104.3	16.0	26	34	36	0.09	0.01
		M-2	780	6.24	107.8	17.5	27	37	40	0.11	0.01
		M-3	1,255	6.15	127.0	17.8	35	48	51	0.15	0.02
		M-4	1,712	6.05	141.9	18.6	41	59	59	0.18	0.02
		M-5	2,200	5.27	137.8	19.3	49	72	69	0.22	0.02

Table 6. Modeled results of the total AMD flux. Numerical values are for high (top) and low (bottom) rainfall days. The actual AMD flux values for the former and latter were 3.47 and 2.62 $m^3\ min^{-1}$, respectively.

Hydraulic conductivity k ($m\ s^{-1}$)		Neogene volcanic rocks			
		3.3×10^{-9}	3.5×10^{-8}	4.8×10^{-8}	2.1×10^{-7}
Faults	1.0×10^{-7}	0.60	2.73	3.43	9.88
		0.46	2.10	2.66	8.23
	2.5×10^{-6}	0.98	3.02	3.67	10.06
		0.70	2.31	2.86	8.37
	1.0×10^{-5}	1.60	3.52	4.11	10.48
		1.06	2.67	3.21	8.68
	1.0×10^{-4}	3.67	5.85	6.54	13.95
		3.03	4.23	5.08	10.77

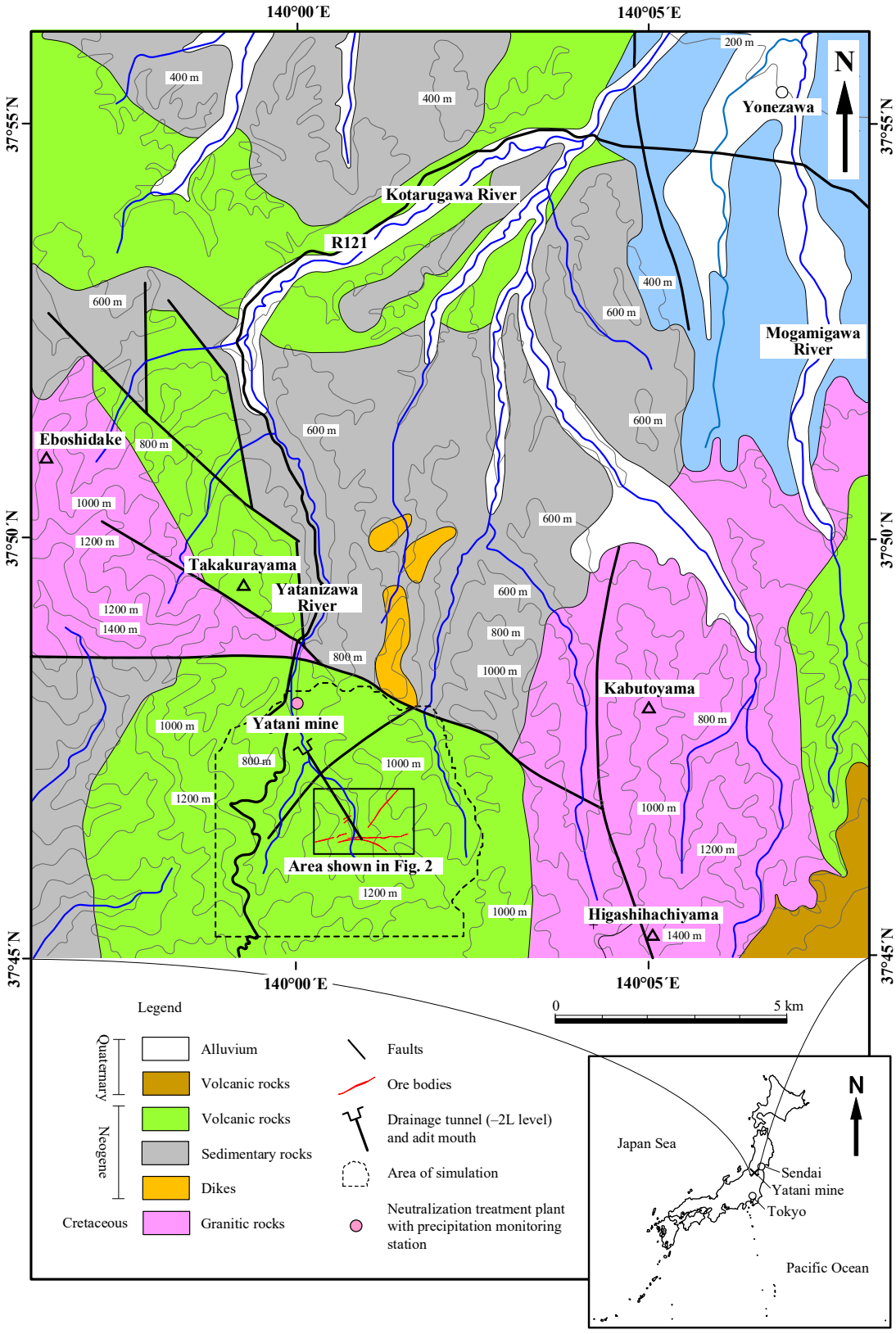

Fig. 1. Geological map and location of the Yatani mine area, with the inset showing its location on a map of Japan. The contour intervals are 200 m.

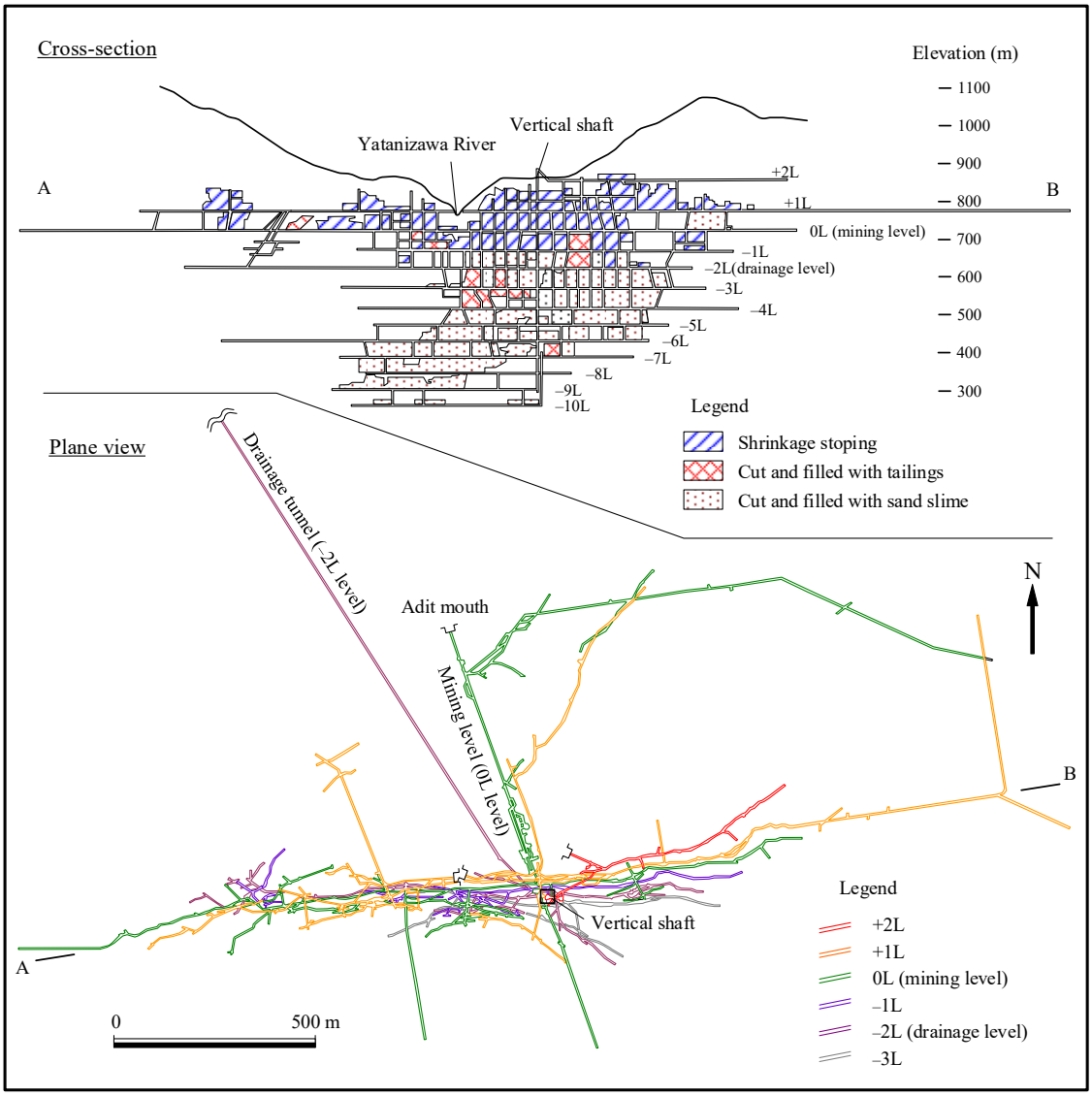

Fig. 2. Distribution of old mine workings and excavated areas of the Yatani mine.

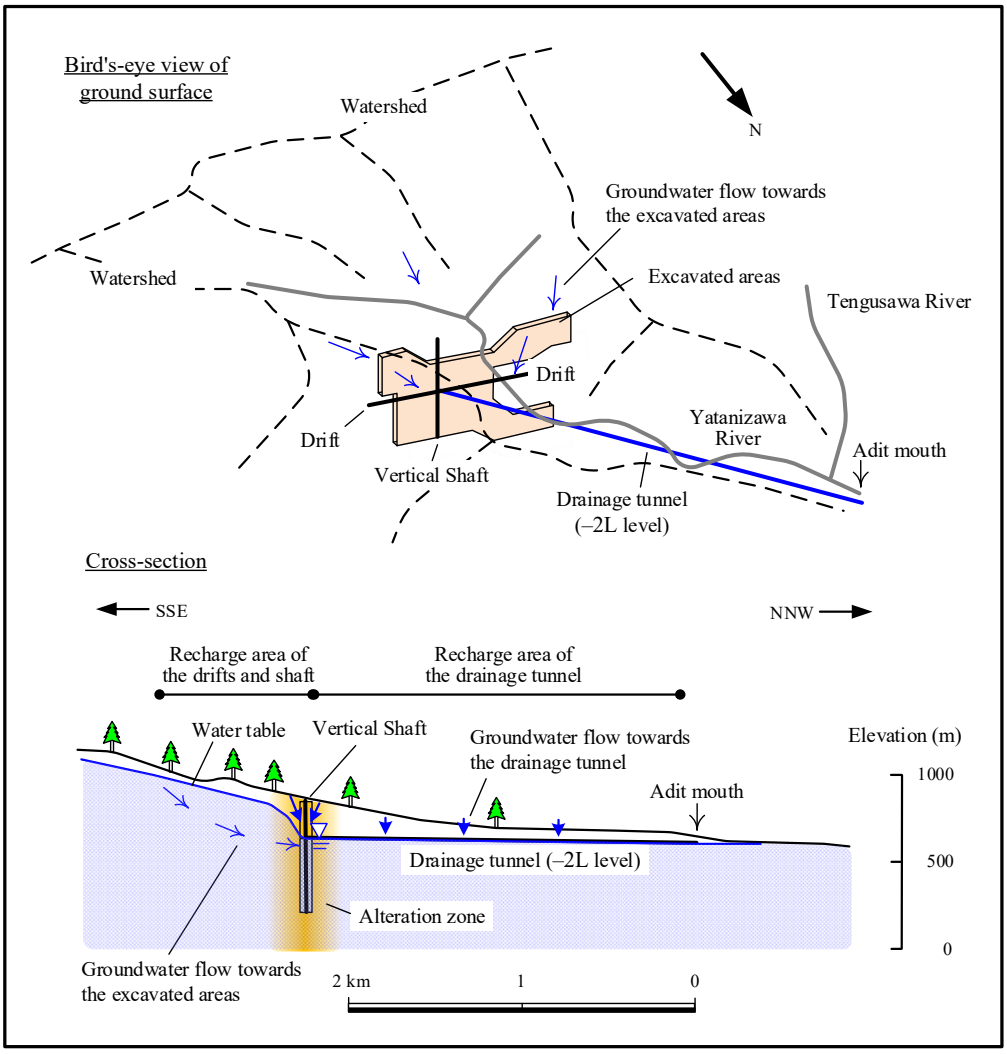

Fig. 3. Conceptual model of groundwater flow and discharge (Tomiyama et al., 2019).

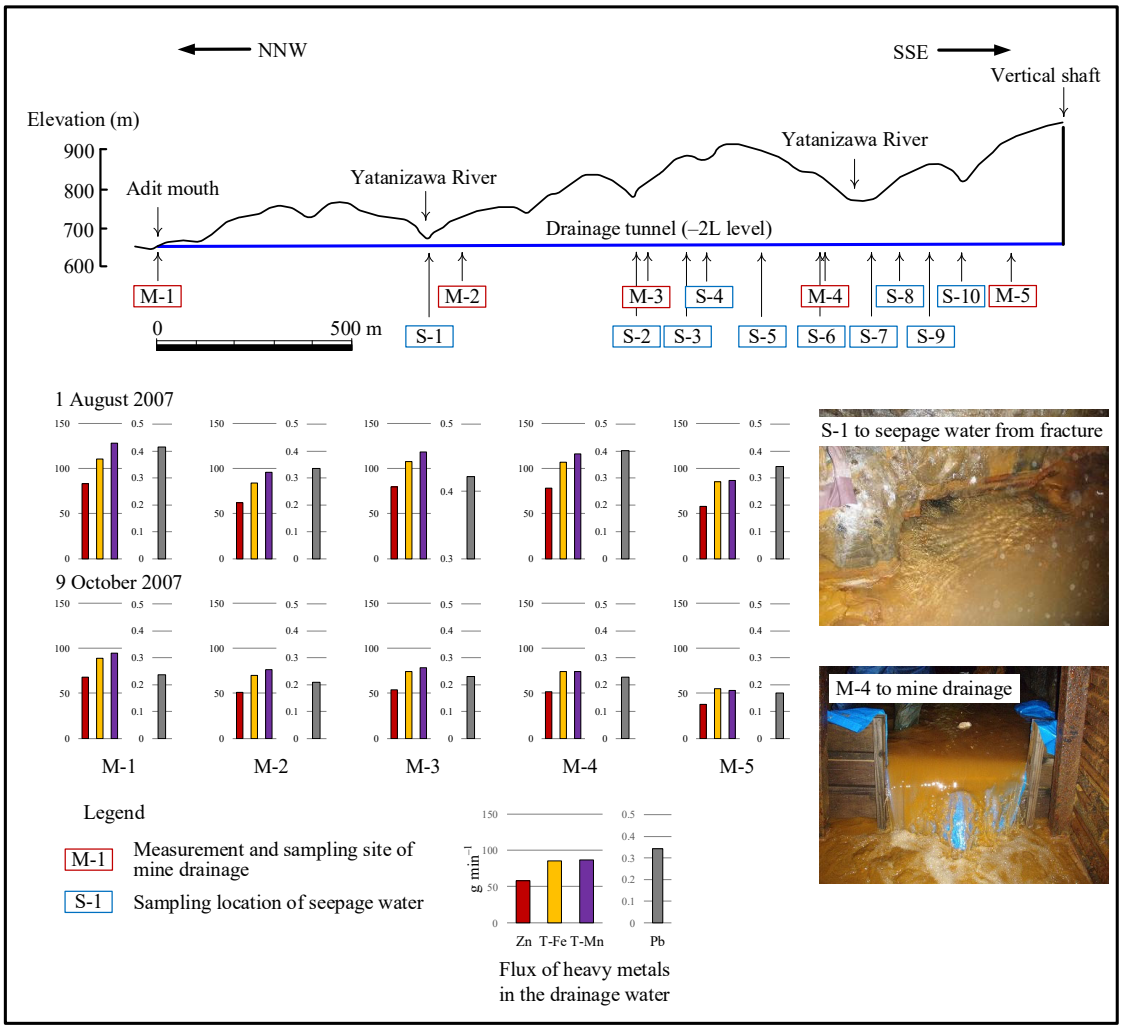

Fig. 4. Location of water sampling sites in the drainage tunnel and flux of heavy metals (Zn, T-Fe, T-Mn, and Pb) in the drainage water. The flux values were calculated by multiplying the concentration by the flow volume of mine drainage.

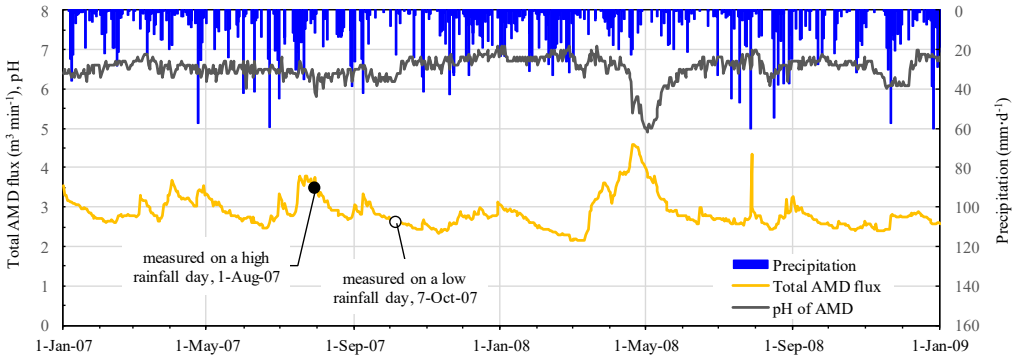

Fig. 5. Relationship between precipitation and total AMD flux, and pH measured at the neutralization treatment plant.

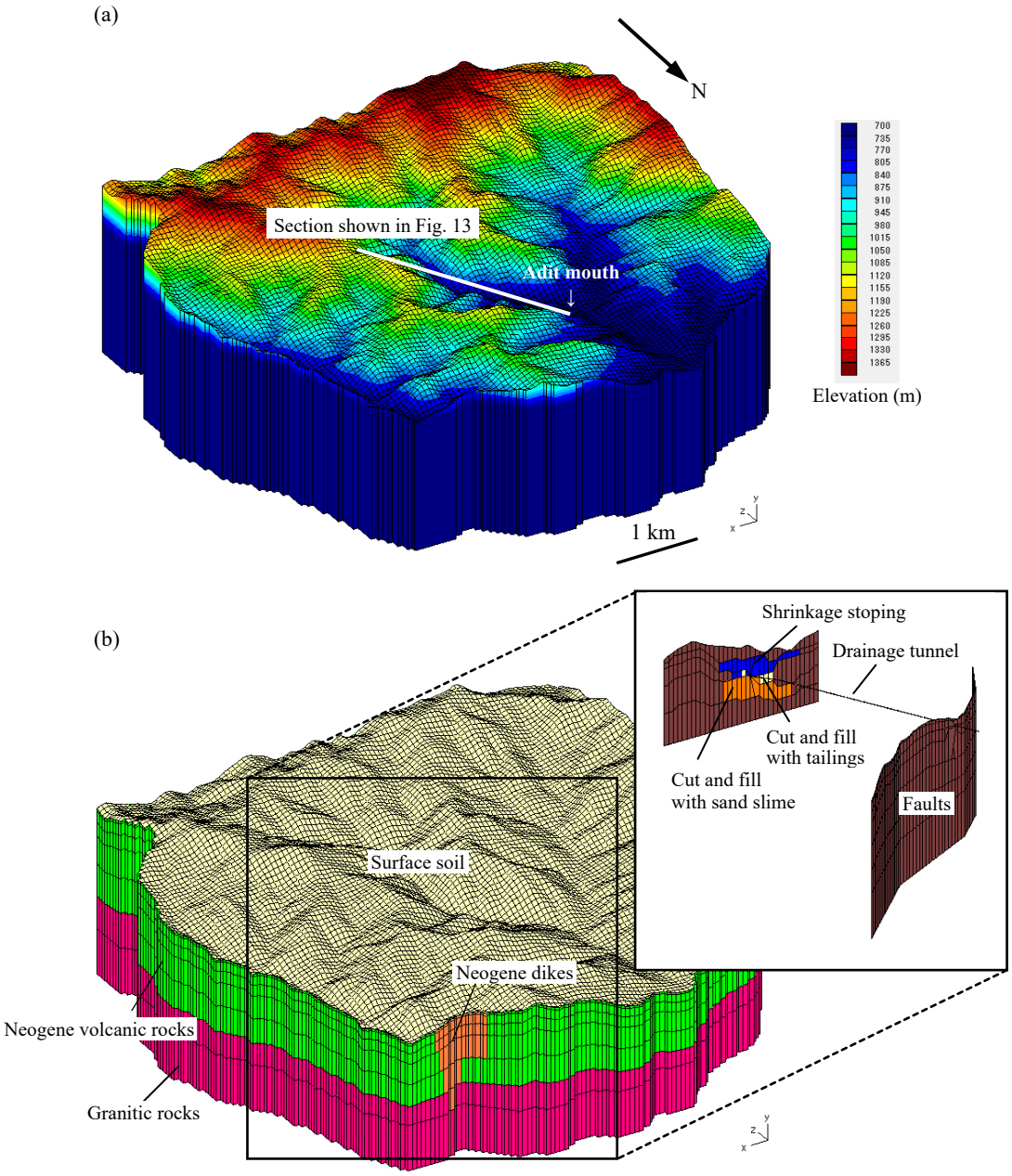

Fig. 6. Model of the three-dimensional groundwater flow. (a) Bird's-eye view of the modeled groundwater flow, and (b) Geological model.

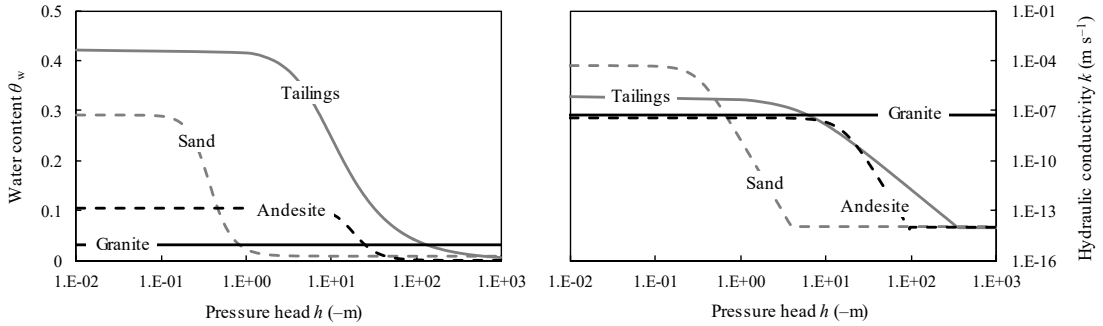

Fig. 7. Water content and hydraulic conductivity curves obtained using van Genuchten's (1980) model for sand slime, tailings, andesite, and granite. See Table 2 for the corresponding parameters of van Genuchten (1980).

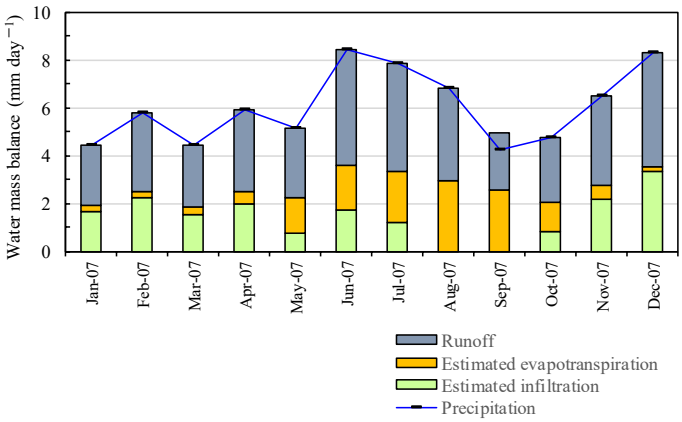

Fig. 8. Water mass-balance values for each month of 2007.

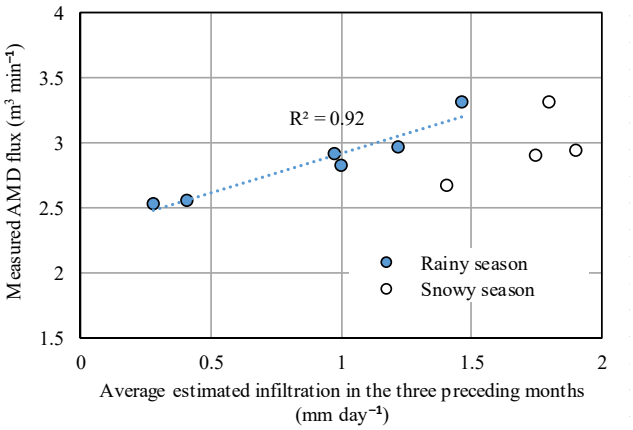

Fig. 9. Relationship between the measured AMD flux of each month and the average estimated infiltration in the three preceding months. The AMD flux is shown from March 2007 to December 2007.

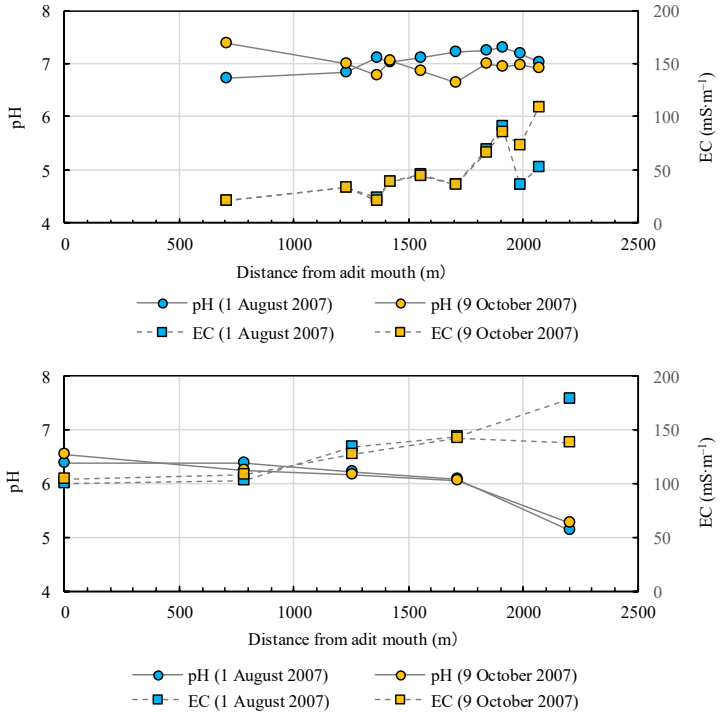

Fig. 10. Spatial variations in the pH and EC of seepage water (top) and mine drainage (bottom) samples along the drainage tunnel.

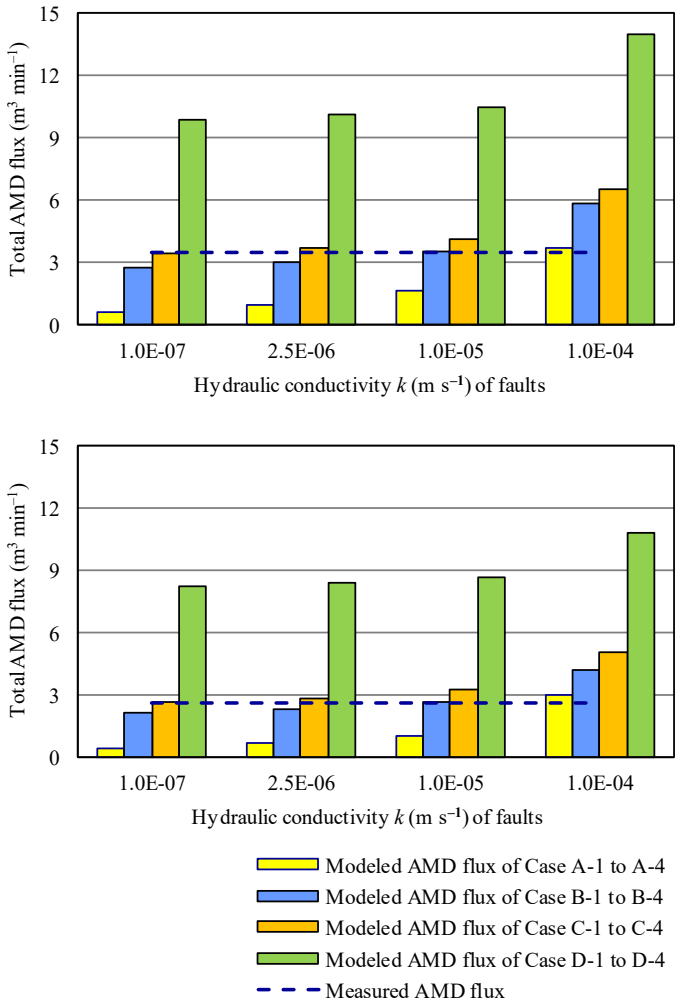

Fig. 11. Relationship between the modeled and measured AMD flux of high (top) and low (bottom) rainfall days.

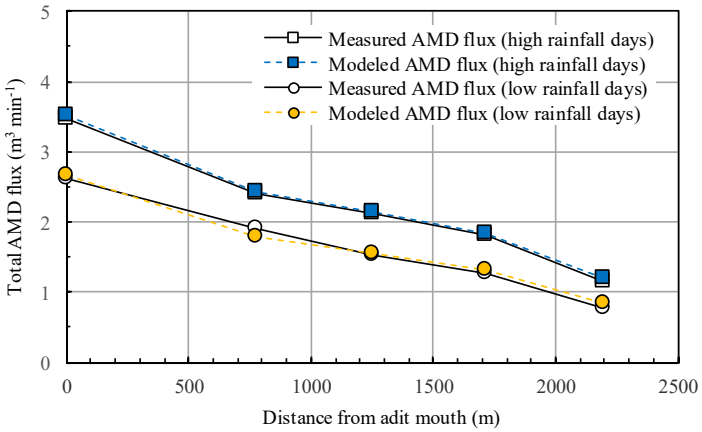

Fig. 12. Relationship between the AMD fluxes predicted by the numerical model and those measured on-site for Case B-3 (where hydraulic conductivities (k) of rock and faults were 3.5×10^{-8} m s^{-1} and 1.0×10^{-5} m s^{-1}, respectively).

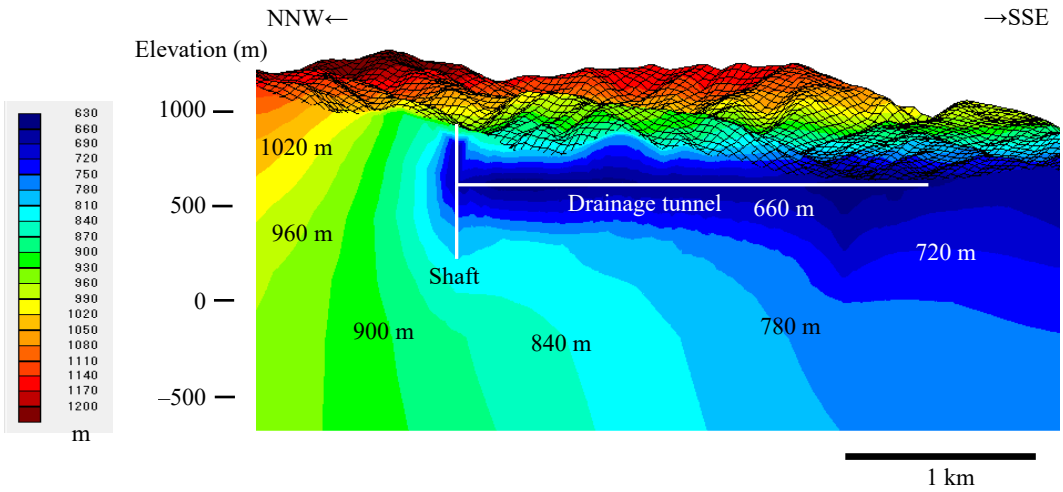

Fig. 13. Distribution of modeled total heads.

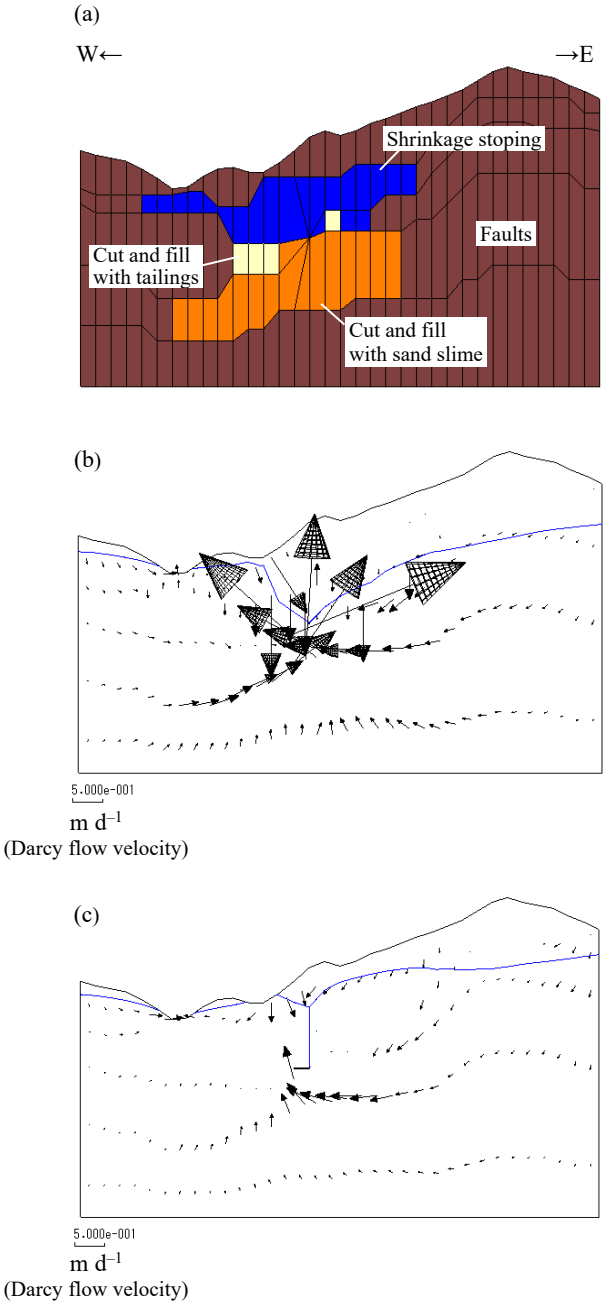

Fig. 14. Effects of filling the excavated areas. (a) Geological model of the three-dimensional groundwater flow around the excavated areas; (b) Distribution of the groundwater flow vectors for Case B-3(where hydraulic conductivities (k) of rock and faults were 3.5×10^{-8} m s^{-1} and 1.0×10^{-5} m s^{-1}, respectively), and (c) Distribution of the groundwater flow vectors after filling the shrinkage stoping areas.